Tin Halide Perovskite Solar Cells with Open-Circuit Voltages Approaching the Shockley-Queisser Limit

Wentao Liu,[a] Shuaifeng Hu,[a] Jorge Pascual,[a] Kyohei Nakano,[b] Richard Murdey,[a] Keisuke Tajima,[b] and Atsushi Wakamiya[,a]*

[a]Institute for Chemical Research, Kyoto University, Gokasho, Uji, Kyoto 611-0011, Japan.

[b]RIKEN Center for Emergent Matter Science (CEMS), Wako, Saitama 351-0198, Japan.

KEYWORDS: solar cell, tin perovskite, electron transport material, energy disorder, solvent engineering

ABSTRACT: The power conversion efficiency of tin-based halide perovskite solar cells is limited by large photovoltage losses arising from the significant energy-level offset between the perovskite and the conventional electron transport material, fullerene C_{60}. The fullerene derivative indene-C_{60} bisadduct (ICBA) is a promising alternative to mitigate this drawback, owing to its superior energy level matching with most tin-based perovskites. However, the less finely controlled energy disorder of the ICBA films leads to the extension of its band tails that limits the photovoltage of the resultant devices and reduces the power conversion efficiency. Herein, we fabricate ICBA films with improved morphology and electrical properties by optimizing the choice of solvent and the annealing temperature. Energy disorder in the ICBA films is substantially reduced, as evidenced by the 22 meV smaller width of the electronic density-of-states. The resulting solar cells show open-circuit voltages of up to 1.01 V, one of the highest values reported so far for tin-based devices. Combined with surface passivation, this strategy enabled solar cells with efficiencies of up to 11.57%. Our work highlights the importance of controlling the properties of the electron transport material towards the development of efficient lead-free perovskite solar cells and demonstrates the potential of solvent engineering for efficient device processing.

INTRODUCTION

Hybrid metal halide perovskite solar cells (PSCs) have become a burgeoning research field owing to the rapid improvement in their power conversion efficiency (PCE) during the past decade, with certified values above 25%.[1–6] Despite this impressive progress, the toxicity of Pb currently limits the commercialization of this technology.[7,8] In this sense, several endeavors have been made to develop PSCs with environment-friendly elements, such as Sn, Ge, Cu, etc.[9–13] In particular, thanks to its superior photophysical properties, Sn is regarded as the most promising substitute for lead in efficient PSCs[14–18] The highest reported efficiency of Sn-based PSCs is, however, less than 15%,[19,20] still far lower than that of their Pb counterparts and well below their theoretical maximum value.[21] One main factor of the efficiency deficit is the large open-circuit voltage (V_{OC}) losses, primarily induced by the energy level mismatch, in particular between the conduction band minimum (CBM) of the Sn-based perovskite films and the lowest unoccupied molecular orbital (LUMO) level of the conventional electron transport material (ETM), C_{60}.[22,23] The community has attempted to address this issue from both the perspective of the perovskite and electron transport materials.[24–28] For perovskites, strategies like composition engineering,[20,29,30] interfacial modification[31,32] and internal structural modulation[33,34] have been developed to fabricate perovskites films with more compatible energy levels with respect to the ETLs. Meanwhile, Jiang et al. replaced C_{60} with indene-C_{60} bisadduct (ICBA) to reduce the energy

barrier at the interface. The shallower LUMO level of ICBA compared to [6,6]-phenyl-C_{61}-butyric acid methyl ester ($PC_{61}BM$) and C_{60} resulted in Sn-based PSCs with an improved efficiency of 12.4% and V_{OC} values of up to 0.94 V.[23]

Despite some promising reports highlighting the superiority of ICBA in Sn-based PSCs,[19,20,35] few laboratories have managed to adopt it so far. A clearer understanding of the fabrication process and its role in determining the characteristics of the ICBA films would open the door to a more extensive implementation. For the case of fullerene derivatives, the deposition procedure strongly determines the final properties of the fullerene film.[36] Energy disorder of organic semiconductors has been comprehensively confirmed to account for the energy loss in organic solar cells.[36,37] Likewise, it has also been reported that significant energy disorder in fullerene derivatives would also limit the performance of the PSCs largely by inducing the V_{OC} loss.[38,39]

Energy disorder is inherent to interacting organic molecules assembled with relatively weak van der Waals forces.[40] The weak electronic interactions between the orbitals of adjacent lattices result in a broadened electronic density of states (DOS) extending into the forbidden gap.[41,42] Various factors, such as undesirable film morphology,[43] phase impurity,[44] and disordered chemical structure,[45,46] can further broaden the distribution of energy states and increase the density of electronic trap states. Strategies like solvent annealing[39] and purification of fullerene derivatives[38] have been examined to successfully mitigate the energetic disorder of ETM films in PSCs. Recently, Jiang et al. achieved a PCE of over

23% in Pb-based inverted PSCs by replacing the $PC_{61}BM$ with a new fullerene derivative, denoted as FP-C8.[47] The energy disorder of the FP-C8 films was reported to be reduced due to the chelation of the pyridine terminal toward the perovskite underneath. Accordingly, we expect that reducing the energy disorder of the ETM films could bring further improvements to the V_{OC} in Sn-based perovskite PSCs.

In this work, we studied the pivotal role of the processing solvent and annealing temperature on the energy disorder of the ICBA films and the resultant device performance. ICBA films were deposited on freshly prepared Sn perovskite films by spin coating using pure and mixed solvents. For the Sn perovskite, we chose the mixed-phase 2D/3D material ($PEA_{0.15}FA_{0.85}SnI_3$) as its superior ability on achieving Sn PSCs with high efficiency.[23,48] Under the optimal fabrication conditions, i.e., chlorobenzene /1,2,4-trichlorobenzene (CB/TCB = 10/1, v/v) as the mixed solvent, the energy disorder of the deposited ICBA films was reduced to 80% of the value obtained with pure CB solvent, and the power conversion efficiencies of the corresponding solar cell devices increased. The energy disorder could be further reduced by increasing the annealing temperature of the ICBA films from 70 to 100 °C. Thanks to the substantially mitigated energy disorder in the ICBA films, the cells exhibited V_{OC} values of up to 1.01 V, which is one of the highest reported cell voltages so far for Sn-based PSCs. In addition, this strategy enabled solar cells with efficiencies of up to 11.57%.

RESULTS AND DISCUSSION

Design strategy

As the energetic disorder in organic semiconductors is greatly affected by the method used to prepare the film,[36] we focused on the fabrication process of the ICBA films, where the selection of solvents plays an essential role.[49–52] For our study we used two aromatic solvents, CB and 1,2-dichlorobenzene (*o*-DCB), which have been previously used to prepare ICBA films,[23,38] and, in addition, another analog with a higher boiling point, TCB. The chemical structures and physical property data are given in the supporting information (**Figure S1 and Table S1**). To modulate the drying period, either *o*-DCB or TCB solvents with relatively low vapor pressures and high boiling points were added to CB in different ratios. This approach would allow the molecules more time to assemble as the residual solvent evaporates during the annealing process.[52] Initially, as-prepared ICBA solutions were spin-coated onto the perovskite films followed by annealing at 70 °C for 10 min, according to the previously reported routine procedure.[23] However, to completely remove TCB (solvent with the highest boiling point, 213.5 °C, and lowest vapor pressure, 0.13 kPa) after spin-coating, we determined that the annealing temperature needed to be increased to 100 °C (**Figure 1a**).

Film morphology

Achieving a good film morphology is crucial for maximizing the transport properties of the ETM,[53–55] thus we used scanning electron microscopy (SEM) to screen ICBA films fabricated from various solvent ratios: 1/0, 4/1, 1/1, 1/4, and 0/1 (v/v) for CB/*o*-DCB, and

1/0, 20/1, 10/1, 5/1, and 0/1 (v/v) for CB/TCB. The SEM images of the ICBA films are shown in **Figure S2**. Of all the films, those processed with CB/*o*-DCB (1/1, v/v) (process afterward referred to as **CD-70**) and CB/TCB (10/1, v/v) (process afterward referred to as **CT-70** or **CT-100** for the films annealed at 70 and 100 °C, respectively) had the best homogeneity and were selected for further evaluation. As a reference, we also prepared films processed from pure chlorobenzene solvent (afterward referred to as **CB-70**). As shown in **Figure 1b**, all four processes (**CB-70**, **CD-70**, **CT-70**, and **CT-100**) lead to ICBA films with full coverage. White islands are observed at the surface of the reference film fabricated from **CB-70**. Considering similar observations made in previous studies,[56,57] these might be ICBA aggregates. The morphological inhomogeneity caused by these large, island-like aggregates may result in increased structural disorder and reduced electron mobility.[58,59] Meanwhile, films processed from **CD-70** and **CT-70** show improved homogeneity. Increasing the annealing temperature to 100 °C did not greatly change the morphology, as confirmed by the similar results for both **CT-70** and **CT-100** processes. Although we conducted X-ray diffraction (XRD) measurements to evaluate the crystallinity of the ICBA films on glass substrates processed under the different fabrication conditions, no discernable XRD peaks were detected (**Figure S3**). The results suggest that all the ICBA films are either amorphous or possess very low levels of crystalline ordering.

To characterize the surface roughness of the films we performed atomic force microscopy (AFM) measurements of ICBA films processed in different conditions. As shown in **Figure 1c**, the root-mean-square (RMS) surface roughness of the films processed from **CB-70**,

CD-70, and **CT-70** films was 4.76, 7.50, and 4.28 nm respectively. Increasing the temperature from 70 to 100 ºC did not lead to significant changes in roughness in **CT-100** processed films. ICBA films obtained from mixed solvents were also more uniform than those obtained from either pure *o*-DCB or pure TCB (**Figure S4**), confirming the positive effect of combining CB with higher boiling point solvents. The improved uniformity is likely due to the balanced evaporation rates.[57] We anticipate that the improved film morphology may lead to a reduced energy disorder of the ICBA films.[52,60–62]

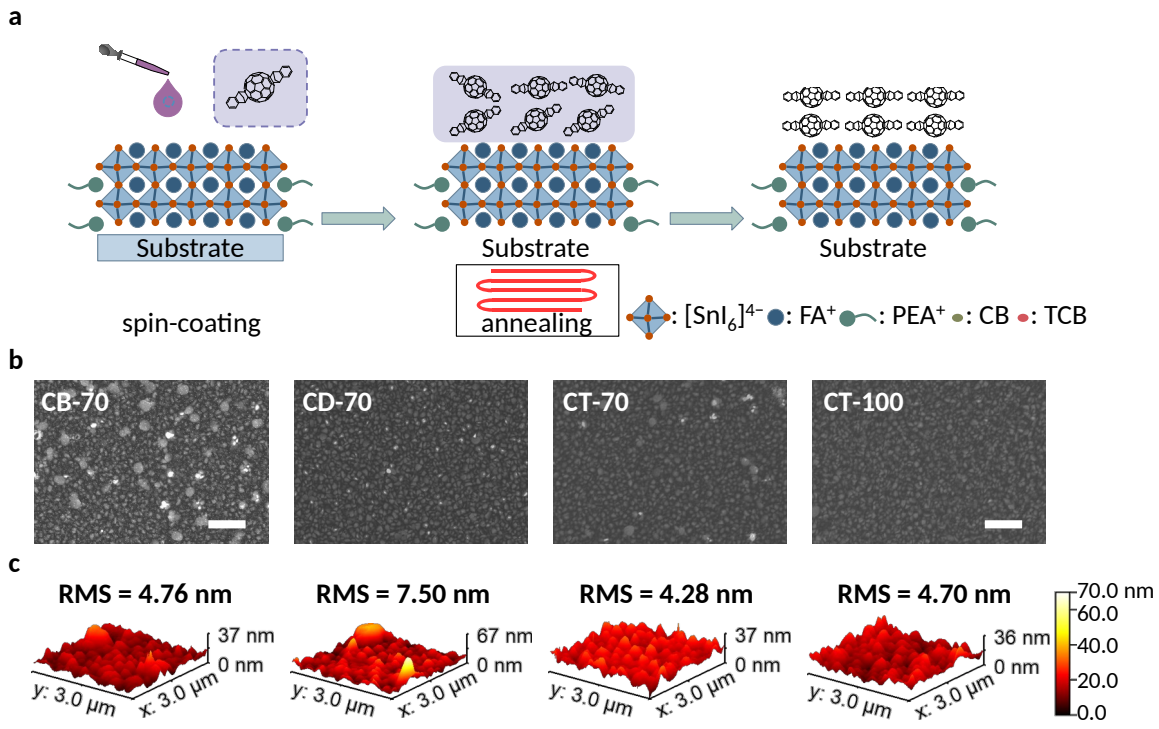

Figure 1. (a) Schematic illustration of the ICBA film fabrication processes. (b) SEM (scale bars are 2 µm) and (c) AFM images of ICBA films fabricated with chlorobenzene (**CB-70**)

annealed at 70 °C, CB/*o*-DCB, 1/1, v/v (**CD-70**) annealed at 70 °C, and CB/TCB,10/1, v/v annealed at 70 (**CT-70**) and 100 °C (**CT-100**).

Energy disorder of the ICBA films

In organic semiconductor films, the DOS can be described by a Gaussian model with function (1),[63]

$$G_n = \frac{N}{\sqrt{2\pi}\sigma} \exp\left[\frac{-\xi^2}{2\sigma^2}\right] (1)$$

where N is the total density of transport sites, ξ the center of the DOS, and σ is generally assumed to be the energy disorder parameter that represents the width of the DOS. In this model, the carrier transport inside a disordered organic semiconductor is regarded as the hopping motion process between localized sites. Since the carrier mobility (μ) is a function of temperature (T) and field (F), it will thus be solely temperature-dependent under a low applied electric field.[63] Combined with a Gaussian disorder model, the energy disorder parameter (σ) can be calculated via a non-Arrhenius type temperature dependence,[63,64]

$$\mu(T) = \mu_\infty \exp\left(-\left(\frac{\sigma}{k_B T}\right)^2\right) (2)$$

where μ_∞ is the mobility as the temperature approaches infinity, k_B is the Boltzmann constant and T is the temperature. In this sense, a more disordered semiconductor will exhibit stronger correlations between mobility and temperature than a less disordered one.

Energy disorder in polycrystalline organic semiconductors, as evidenced by a broadened Gaussian DOS, can be correlated to increased structural disorder in the material.[36] To evaluate the solvent and annealing effects of ICBA films on energy disorder, we measured the space-charge limited current (SCLC)[47] in electron-only ITO/ZnO/ICBA/BCP/Ag devices (ITO stands for indium tin oxide, ZnO for zinc oxide, and BCP for bathocuproine) in the dark at temperatures between 213 and 273 K (**Figure 2a-d**). The electron mobilities (μ_e) were calculated using the Mott-Gurney equation fitted to the data region where second-order current-voltage behavior, i.e. $J = V^2$ was observed (**Figure S5**).[65] As shown in **Figure 2a-d**, when the temperature was decreased from 273 to 213 K, the electron mobility of the films processed from **CB-70** and **CD-70** decreased from 1.65×10^{-7} to 1.34×10^{-9} $cm^2\ V^{-1}\ s^{-1}$ and from 8.88×10^{-3} to 6.44×10^{-6} $cm^2\ V^{-1}\ s^{-1}$ respectively. In contrast, the **CT-70** processed ICBA films exhibited a weaker temperature dependence for mobility, falling from 4.11×10^{-5} to 2.38×10^{-6} $cm^2\ V^{-1}\ s^{-1}$. The temperature dependence was even weaker in ICBA films processed from **CT-100**, with μ_e decreasing from 7.76×10^{-4} to 1.24×10^{-4} $cm^2\ V^{-1}\ s^{-1}$. As a stronger dependence of the mobility on temperature indicates a larger energy disorder,[64] these results suggest that the energy disorder of ICBA films processed from **CT-100** was greatly mitigated, especially when compared to the **CB-70** and **CD-70** processed ones. The energy disorder parameters for ICBA films processed from **CB-70**, **CD-70**, **CT-70**, and **CT-100**, calculated with equation (2), are 58, 74, 46, and 36 meV, respectively (**Figure 2e**). Given that the energy level offsets between the perovskite conduction band and the ICBA LUMO was estimated to be largely unchanged for the four

films, we attribute the V_{OC} loss to the different degree of energy disorder of the ETL films,[38] as illustrated in **Figure 2f** (Detailed discussion is provided in Supporting Information **Figures S6-S12**). The broadened DOS and extended band tails caused by the increased energy disorder introduce additional traps in the forbidden gap, which can act as recombination centers that reduce the quasi-Fermi energy level and increase the V_{OC} loss.[38,39] In this framework, the reference **CB-70** process as well as the **CD-70** one resulted in relatively high energy disorder, which we anticipate to translate into a significant V_{OC} loss in the corresponding solar cells. In comparison, the energy disorder in the **CT-70** and **CT-100** processed films was significantly lower.

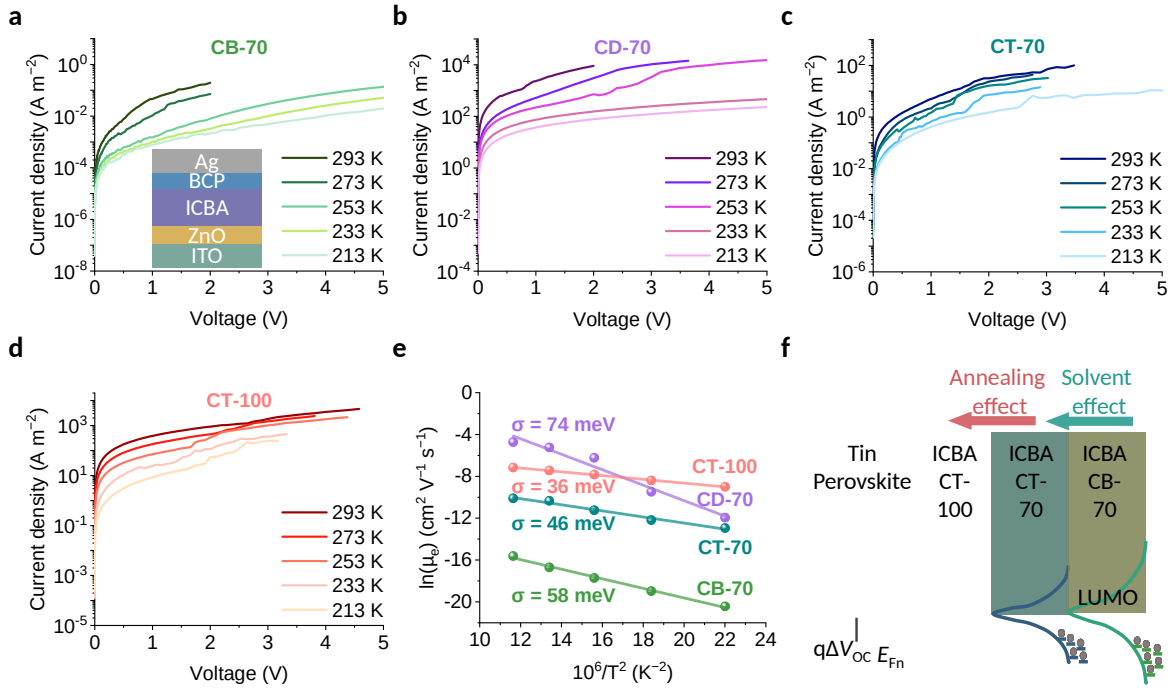

Figure 2. Temperature dependence of electron transport for electron-only devices with ICBA films processed from (a) **CB-70**, (b) **CD-70**, (c) **CT-70**, and (d) **CT-100**. Inset shows

the device structure. (e) Temperature dependence of electron mobility. (f) Schematic illustration of the solvent and annealing effect on the energy disorder, quasi-Fermi level (E_{Fn}), and V_{OC}.

Device performance

We fabricated solar cells with the device architecture of ITO/PEDOT:PSS/$PEA_{0.15}FA_{0.85}SnI_3$/ICBA/BCP/Ag (**Figure 3a**), where PEDOT:PSS stands for poly(3,4-ethylenedioxythiophene):poly(styrene sulfonate). The active area of the cells, determined by the shadow mask, was 0.0985 cm^2.

Device performance was evaluated to confirm the optimal solvent ratios. The statistical distributions of performance parameters for devices with ICBA films processed with CB/*o*-DCB and CB/TCB mixed solvents are given in **Figures S13-S14**. For mixed CB/*o*-DCB solvent, the solvent ratio of 1:1 (v/v) was confirmed to result in devices with the best PCE, short-circuit current density (J_{SC}), and fill factor (FF). The V_{OC} decreased as the fraction of *o*-DCB increased. For mixed CB/TCB solvent, ICBA films fabricated with the solvent ratio of 10:1 (v/v) resulted in devices with the best PCE, V_{OC}, and FF values, while the optimum J_{SC} was obtained at the ratio of 5:1. In terms of PCE, the optimal solvent ratios for processing the ICBA films were 1:1 (v/v) for CB/*o*-DCB and 10:1 (v/v) for CB/TCB mixed solvents, in line with the previous evaluation of the improved film morphology.

Subsequently, we fabricated devices based on ICBA films processed from **CB-70**, **CD-70**, **CT-70**, and **CT-100**. The typical *J-V* curves are shown in **Figure 3b** and the corresponding *J-V* parameters are given in **Table S2**. For the ICBA films processed from **CB-70**, the champion devices exhibited V_{OC} values of 0.77 V (PCE = 7.73%, J_{SC} = 15.04 mA cm^{-2}, and FF = 0.67). For the films processed from **CD-70**, the resulting V_{OC} decreased to 0.64 V (PCE = 8.72%, J_{SC} = 19.22 mA cm^{-2}, and FF = 0.71). Meanwhile, the **CT-70** processed ICBA films led to increased V_{OC} of up to 0.81 V (PCE = 8.74%, J_{SC} = 15.32 mA cm^{-2}, and FF = 0.70), with the stabilized power output of 8.1% after 1000 s operation (**Figure S15**). The **CT-70** process yielded Sn-based PSCs with improved reproducibility as well, evident from the narrower distribution of the cell performances presented in **Figure S16**. As discussed above, the change in V_{OC} can be ascribed to the variation of energy disorder. The ICBA films processed from **CD-70** mixed solvent exhibited the most severe energy disorder, leading to the lowest V_{OC} in devices among all the cases examined. Meanwhile, the superior J_{SC} of **CD-70** films might originate from their highest room-temperature mobility (**Figure 2e and 3b**). In contrast, the ICBA films processed from **CT-70** showed mitigated energy disorder with a narrowed width of DOS, leading to their higher V_{OC} in the solar cells.

The V_{OC} of the devices with ICBA layers processed from **CT-100** was even higher than for the **CT-70** processed ICBA layers, consistent with the minimized energy disorder of the related films. As a result, the devices reached V_{OC} values of up to 1.01 V (**Figure 3b and**

3c). This value of V_{OC} is one of the best so far reported for Sn-based PCSs (**Figure 3d**).[9,19,20,23,29,35,66–79] Nonetheless, the efficiency decreased to 3.90% due to the lower J_{sc} of 6.59 mA cm^{-2}. The external quantum efficiency (EQE) also decreased, though the bandgap of 1.44 eV was essentially unchanged (**Figure 3e**).

Additional tests were conducted to confirm the dependence of J_{SC} on the processing temperatures (**Figure S17**). Since the drying step for ICBA films also heats the perovskite layers underneath, we fabricated devices where the perovskite films were treated with a second annealing step at either 70 or 100 °C before depositing the top layers (**Figures S18-S20**). The cells with the perovskite films treated at 70 ºC did not experience significant losses in the photovoltaic parameters, while the ones annealed at 100 °C suffered strong losses on the PCE due to a dramatic decrease in the J_{SC}, but maintained quite comparable V_{OC} values. These tests demonstrate that the current loss originates from the high temperatures experienced by the perovskite layer, while the increase in cell voltages arises from the higher temperatures experienced by the perovskite/ICBA system. Unlike 3D tin perovskite films, which are usually annealed at 100 °C, thermal stress can cause significant changes in the chemical composition and structure of mixed dimensional perovskite films.[80] High efficiency, mixed dimensional 2D/3D tin-based perovskite solar cells are therefore generally fabricated under temperatures not higher than 80 °C.[19,23,35] XRD measurements were used to characterize the effect of the annealing temperature on perovskite films deposited on PEDOT:PSS/ITO substrate. As shown in **Figure S21**, the intensity of the

(100) peak of the films annealed at 100 °C was significantly lower than the films annealed at 70 °C, while no new peaks or peaks shifts were observed, suggesting that the higher annealing temperature induced a significant loss of crystalline order. We conclude that while there appears to be no decomposition of the perovskite at elevated annealing temperatures, the overall loss of crystallinity is the most likely cause of the decreased current density.[81,82] Since the highest cell voltages were realized at elevated temperatures, increasing the robustness of the perovskite films against thermal stress is essential for increasing the PCE.

Considering the bandgap of 1.44 eV, the V_{OC} of 1.01 V obtained for the device with the **CT-100** processed ICBA layer is 0.15 V lower than Shockley-Queisser (SQ) limit.[21,83–85]. The ICBA films with reduced energy disorder have fewer extra tail states to trap photo-generated electrons at the perovskite/ICBA interface, resulting in fewer non-radiative recombination events and higher V_{OC}.[86] The suppression of trap-mediated charge carrier recombination can be characterized using the ideality factor (n_{id}) determined from the slope of the light intensity-V_{OC} plot. As shown in **Figure 3f**, the n_{id} values are 1.79, 1.43, and 1.39 for devices with ICBA films fabricated from **CD-70**, **CB-70**, and **CT-70** processes, respectively, and 1.24 with the ICBA film processed from **CT-100**. The lower energy disorder results in a n_{id} closer to unity, expected for the suppression of the trap-assisted recombination at the perovskite/ICBA interface, and in line with the enhanced V_{OC} of the corresponding solar cells.[27,87]

We examined the shelf-stability of the unencapsulated Sn-based PSCs with **CB-70**, **CD-70**, and **CT-70** processed ICBA films. For this test, the devices were stored in the dark in an N_2-filled glovebox. We found that devices with ICBA film processed from **CT-70** maintained over 80% of their initial efficiency for over 1300 hours of storage, while devices with **CB-70** and **CD-70** processed ICBA layers retained just 67% (**Figure S22**). Sn-based perovskites, especially their surface regions, are vulnerable to external stimuli,[88] such as oxygen and water. In PSCs with inverted structures, the ETL can generally act as a barrier to protect the perovskite film underneath from detrimental invasion.[60] Thus, a denser, less permeable, or more hydrophobic ETL can improve the storage life.[47] The layers processed from **CT-70** displayed a slightly larger water contact angle of 91.2° compared to that of the films processed from **CB-70** (89.3°) and **CD-70** (89.0°) (**Figure S23**), suggesting improved protection of the perovskite films underneath and thus better stability for the corresponding devices.[90]

Considering the PCE and stability, **CT-70** is the optimal process to fabricate Sn-based PSCs without J_{SC} deficit. To further improve the efficiency of devices with ICBA films processed from **CT-70**, we applied the universal post-treatment with ethylenediammonium diiodide ($EDAI_2$) we recently developed.[91,92] The $EDAI_2$-treated solar cells presented superior PCE values of up to 11.57% (J_{SC} = 20.02 mA cm^{-2}, V_{OC} = 0.84, and FF = 0.68) (**Figures S24a and S25**). Although the lower currents are often associated with the 2D components within the perovskite film,[48,81] we found that it was possible to increase the

short circuit current to 20 mA cm^{-2} by using $EDAI_2$ surface treatment. The increased J_{SC} was confirmed with the integrated J_{SC} of 19.42 mA cm^{-2} estimated from external quantum efficiency (EQE) (**Figure S24b**). The enhancement in J_{SC} likely originates from the strengthened crystallinity of treated perovskite films as evident from X-ray diffraction (XRD) measurement (**Figure S26**), in line with the previous report.[91] Despite the remarkable increase after $EDAI_2$ treatment, the V_{OC} of resultant solar cells is still lower than the value of 1.01 V obtained for the **CT-100** processed devices. Therefore, future efforts should focus on improving the endurance of Sn-based perovskites against thermal stress.

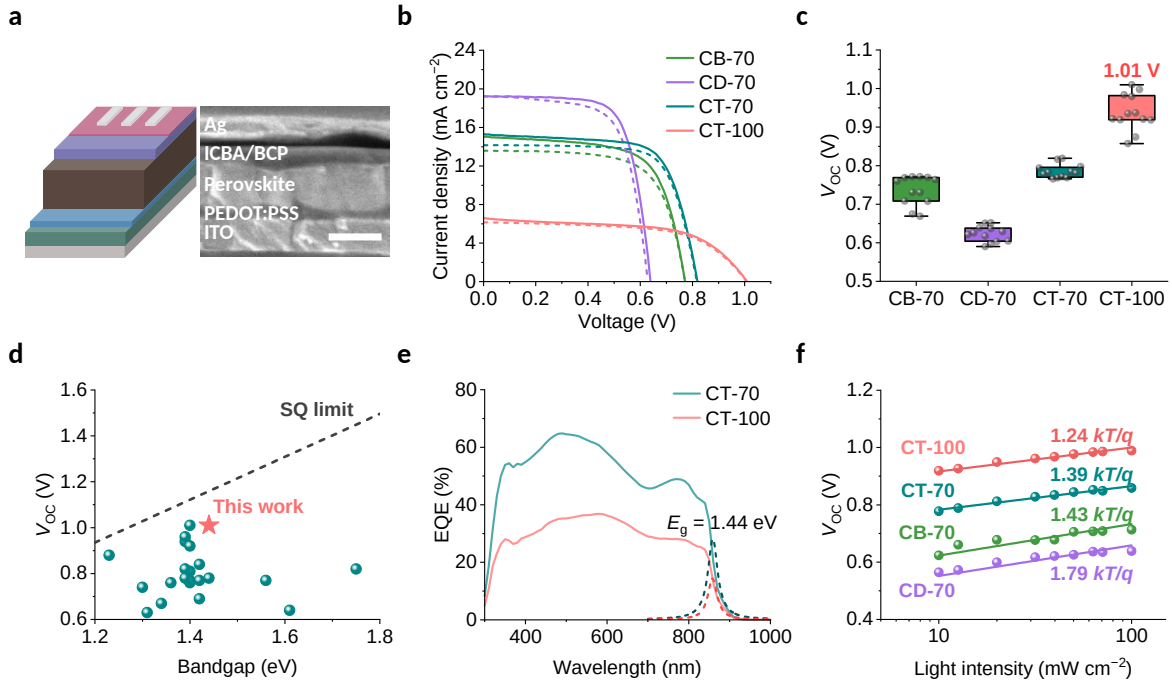

Figure 3 (a) Schematic illustration and cross-section SEM images of devices (scale bars are 250 nm). (b) *J-V* curves of typical devices with ICBA layers fabricated from **CB-70**, **CD-70**, **CT-70**, and **CT-100** processes. Forward and reverse scans are shown with solid and

dashed lines, respectively. (c) Distributions of the V_{OC} values from the cells. (d) V_{OC} values of the Sn-based PSCs reported in this work and previous literature.[9,19,20,23,29,35,66–79] The dashed line indicates the SQ limit. (e) EQE spectra of the devices with **CT-70** and **CT-100** processed ICBA films, the bandgap is estimated from the peak of the differential signal shown with dashed lines. The integrated J_{SC} is 16.78 and 9.88 mA cm^{-2} for devices based on CT-processed ICBA films annealed at 70 and 100 °C, respectively. (f) V_{OC} as a function of illumination intensity for the devices (k is Boltzmann's constant, T is 298 K, and q is the unit of electronic charge).

CONCLUSION

In summary, a solvent engineering strategy was developed to improve the performance of ICBA electron transport layers in 2D/3D Sn-based PSCs. ICBA films were fabricated by spin coating from mixed solutions of *o*-DCB or TCB in CB. Among these, mixtures with TCB exhibited the most favorable effect. ICBA films processed from CB/TCB show improved surface morphology and lower surface roughness, as well as mitigated energy disorder. Non-radiative charge carrier recombination at the perovskite/ETL interface was suppressed and, as a result, the optimized devices exhibited a superior PCE of 8.74%. With the CT-processed ICBA films, we achieved cell efficiencies of up to 11.57% in combination with the surface post-treatment we developed recently. Combined with an elevated annealing temperature from 70 to 100 °C, the V_{OC} reached values up to 1.01 V, 0.15 V below the SQ limit for the bandgap of 1.44 eV, which is the best value reported so

far for PSCs with this bandgap. This work confirms that voltages nearing the radiative limit can be realized in lead-free PSCs, and further suggests that impressive power conversion efficiencies could be realized once the current J_{SC} deficit is overcome. Overall, our work highlights the critical role that structural disorder plays in determining the performance of fullerene-based ETMs in lead-free PSCs and provides useful insights into how solvent engineering can be used to control the structure and electronic properties of the ETM layer.

ASSOCIATED CONTENT

Supporting Information

The Supporting Information is available free of charge at https://pubs.acs.org/doi/XXX.

Experimental section, SEM and AFM images of the perovskite and ICBA films, UPS and absorption spectra of perovskite and ICBA films, *J*-*V* curves of the solar cell devices, device performance parameters with standard deviation, dark *J*-*V* curves of the devices for SCLC measurements, XRD patterns of the perovskite films, shelf-stability test of solar cell devices, water contact angles of the ICBA films (PDF)

AUTHOR INFORMATION

Corresponding Author

Atsushi Wakamiya: wakamiya@scl.kyoto-u.ac.jp

Authors ORCID:

Wentao Liu: 0000-0003-0077-8042

Shuaifeng Hu: 0000-0003-1312-075X

Jorge Pascual: 0000-0001-6486-0737

Kyohei Nakano: 0000-0003-2493-2817

Richard Murdey: 0000-0001-7621-9664

Keisuke Tajima: 0000-0003-1590-2640

Atsushi Wakamiya: 0000-0003-1430-0947

Author Contributions

W. L. and S. H. conceived the idea and designed the experiment; W. L. measured the SEM; R. M. measured AFM; W. L. conducted the XRD measurements with the help of J. P.; W. L. fabricated the solar cell devices and did the related characterizations with the help of S. H. and J. P.; W. L. and S. H. carried out the SCLC measurements and the energy disorder analyses; K. N and K. T conducted UPS measurements. W. L. carried out the optical absorption measurements with the help of S. H. W. L., S. H., and J. P. prepared the manuscript. S. H. and A. W. supervised the project. All authors commented on the manuscript.

Notes

A. W. is co-founder and CSO of Enecoat Technologies Co., Ltd.

ACKNOWLEDGMENTS

This work was partially supported by JST-Mirai Program (JPMJMI22E2) and JST–ALCA (JPMJAL1603) programs, NEDO, JSPS Grant-in-Aid for Scientific Research (A) (21H04699), International Collaborative Research Program of ICR, Kyoto University, ICR Grants for Promoting Integrated Research, Kyoto University, grants for the Integrated Research Consortium on Chemical Sciences, JSPS for a Research Fellowship for Young Scientists (21J14762), and the China Scholarship Council (CSC). We thank Dr. Masato Goto, Tao Fang (Kyoto University), Noriko Kurose (Kyoto University), Prof. Takeshi Hasegawa (Kyoto University) and Prof. Yuichi Shimakawa (Kyoto University) for assistance with XRD measurements, Dr. Nobutaka Shioya and Prof. Takeshi Hasegawa (Kyoto University) for assistance with water contact angle measurement, Yasuko Iwasaki (Kyoto University) for assistance with SEM measurements, Koji Matsumura (Toray Research Center Inc.) for KPFM measurement and Ajinomoto FineTechno Co., Inc. for providing the encapsulation materials.

REFERENCES

(1) Jeong, J.; Kim, M.; Seo, J.; Lu, H.; Ahlawat, P.; Mishra, A.; Yang, Y.; Hope, M. A.; Eickemeyer, F. T.; Kim, M.; Yoon, Y. J.; Choi, I. W.; Darwich, B. P.; Choi, S. J.; Jo, Y.; Lee, J. H.; Walker, B.; Zakeeruddin, S. M.; Emsley, L.; Rothlisberger, U.; Hagfeldt, A.; Kim, D. S.; Grätzel, M.; Kim, J. Y. Pseudo-Halide Anion Engineering

for α-FAPbI3 Perovskite Solar Cells. *Nature* **2021**, *592* (7854), 381–385. https://doi.org/10.1038/s41586-021-03406-5.

(2) Min, H.; Lee, D. Y.; Kim, J.; Kim, G.; Lee, K. S.; Kim, J.; Paik, M. J.; Kim, Y. K.; Kim, K. S.; Kim, M. G.; Shin, T. J.; Seok, S. I. Perovskite Solar Cells with Atomically Coherent Interlayers on SnO2 Electrodes. *Nature* **2021**, *598*, 444–450.

(3) Yoo, J. J.; Seo, G.; Chua, M. R.; Park, T. G.; Lu, Y.; Rotermund, F.; Kim, Y.-K.; Moon, C. S.; Jeon, N. J.; Correa-Baena, J.-P.; Bulovi´c, V.; Shin, S. S.; Bawendi, M. G.; Seo, J. Efficient Perovskite Solar Cells via Improved Carrier Management. *Nature* **2021**, *590*, 587–593.

(4) Zhang, T.; Wang, F.; Kim, H.-B.; Choi, I.-W.; Wang, C.; Cho, E.; Konefal, R.; Puttisong, Y.; Terado, K.; Kobera, L.; Chen, M.; Yang, M.; Bai, S.; Yang, B.; Suo, J.; Yang, S.-C.; Liu, X.; Fu, F.; Yoshida, H.; Chen, W. M.; Brus, J.; Coropceanu, V.; Hagfeldt, A.; Brédas, J.-L.; Fahlman, M.; Kim, D. S.; Hu, Z.; Gao, F. Ion-Modulated Radical Doping of Spiro-OMeTAD for More Efficient and Stable Perovskite Solar Cells. *Science* **2022**, *377* (6605), 495–501. https://doi.org/10.1126/science.abo2757.

(5) Zhao, Y.; Ma, F.; Qu, Z.; Yu, S.; Shen, T.; Deng, H.-X.; Chu, X.; Peng, X.; Yuan, Y.; Zhang, X.; You, J. Inactive (PbI_2)$_2$RbCl Stabilizes Perovskite Films for Efficient Solar Cells. *Science* **2022**, *377* (6605), 531–534. https://doi.org/10.1126/science.abp8873.

(6) Jiang, Q.; Tong, J.; Xian, Y.; Kerner, R. A.; Dunfield, S. P.; Xiao, C.; Scheidt, R. A.; Kuciauskas, D.; Wang, X.; Hautzinger, M. P.; Tirawat, R.; Beard, M. C.; Fenning, D. P.; Berry, J. J.; Larson, B. W.; Yan, Y.; Zhu, K. Surface Reaction for Efficient and Stable Inverted Perovskite Solar Cells. *Nature* **2022**, *611* (7935), 278–283. https://doi.org/10.1038/s41586-022-05268-x.

(7) Abate, A. Perovskite Solar Cells Go Lead Free. *Joule* **2017**, *1* (4), 659–664. https://doi.org/10.1016/j.joule.2017.09.007.

(8) Babayigit, A.; Ethirajan, A.; Muller, M.; Conings, B. Toxicity of Organometal Halide Perovskite Solar Cells. *Nat. Mater.* **2016**, *15* (3), 247–251. https://doi.org/10.1038/nmat4572.

(9) Noel, N. K.; Stranks, S. D.; Abate, A.; Wehrenfennig, C.; Guarnera, S.; Haghighirad, A.-A.; Sadhanala, A.; Eperon, G. E.; Pathak, S. K.; Johnston, M. B.; Petrozza, A.; Herz, L. M.; Snaith, H. J. Lead-Free Organic–Inorganic Tin Halide Perovskites for Photovoltaic Applications. *Energy Env. Sci* **2014**, *7* (9), 3061–3068. https://doi.org/10.1039/C4EE01076K.

(10) Krishnamoorthy, T.; Ding, H.; Yan, C.; Leong, W. L.; Baikie, T.; Zhang, Z.; Sherburne, M.; Li, S.; Asta, M.; Mathews, N.; Mhaisalkar, S. G. Lead-Free Germanium Iodide Perovskite Materials for Photovoltaic Applications. *J. Mater. Chem. A* **2015**, *3* (47), 23829–23832. https://doi.org/10.1039/C5TA05741H.

(11) Saparov, B.; Hong, F.; Sun, J.-P.; Duan, H.-S.; Meng, W.; Cameron, S.; Hill, I. G.; Yan, Y.; Mitzi, D. B. Thin-Film Preparation and Characterization of $Cs_3Sb_2I_9$: A Lead-Free Layered Perovskite Semiconductor. *Chem. Mater.* **2015**, *27* (16), 5622–5632. https://doi.org/10.1021/acs.chemmater.5b01989.

(12) Slavney, A. H.; Hu, T.; Lindenberg, A. M.; Karunadasa, H. I. A Bismuth-Halide Double Perovskite with Long Carrier Recombination Lifetime for Photovoltaic Applications. *J. Am. Chem. Soc.* **2016**, *138* (7), 2138–2141. https://doi.org/10.1021/jacs.5b13294.

(13) Cortecchia, D.; Dewi, H. A.; Yin, J.; Bruno, A.; Chen, S.; Baikie, T.; Boix, P. P.; Grätzel, M.; Mhaisalkar, S.; Soci, C.; Mathews, N. Lead-Free $MA_2CuCl_xBr_{4-x}$ Hybrid Perovskites. *Inorg. Chem.* **2016**, *55* (3), 1044–1052. https://doi.org/10.1021/acs.inorgchem.5b01896.

(14) Stoumpos, C. C.; Malliakas, C. D.; Kanatzidis, M. G. Semiconducting Tin and Lead Iodide Perovskites with Organic Cations: Phase Transitions, High Mobilities, and Near-Infrared Photoluminescent Properties. *Inorg. Chem.* **2013**, *52* (15), 9019–9038. https://doi.org/10.1021/ic401215x.

(15) Ke, W.; Kanatzidis, M. G. Prospects for Low-Toxicity Lead-Free Perovskite Solar Cells. *Nat. Commun.* **2019**, *10* (1), 965. https://doi.org/10.1038/s41467-019-08918-3.

(16) Ke, W.; Stoumpos, C. C.; Kanatzidis, M. G. “Unleaded” Perovskites: Status Quo and Future Prospects of Tin-Based Perovskite Solar Cells. *Adv. Mater.* **2019**, *31* (47), 1803230. https://doi.org/10.1002/adma.201803230.

(17) Fang, H.-H.; Adjokatse, S.; Shao, S.; Even, J.; Loi, M. A. Long-Lived Hot-Carrier Light Emission and Large Blue Shift in Formamidinium Tin Triiodide Perovskites. *Nat. Commun.* **2018**, *9* (1), 243. https://doi.org/10.1038/s41467-017-02684-w.

(18) Abate, A. Stable Tin-Based Perovskite Solar Cells. *ACS Energy Lett.* **2023**, 1896–1899. https://doi.org/10.1021/acsenergylett.3c00282.

(19) Jiang, X.; Li, H.; Zhou, Q.; Wei, Q.; Wei, M.; Jiang, L.; Wang, Z.; Peng, Z.; Wang, F.; Zang, Z.; Xu, K.; Hou, Y.; Teale, S.; Zhou, W.; Si, R.; Gao, X.; Sargent, E. H.; Ning, Z. One-Step Synthesis of SnI2·(DMSO)x Adducts for High-Performance Tin Perovskite Solar Cells. *J. Am. Chem. Soc.* **2021**, *143* (29), 10970–10976. https://doi.org/10.1021/jacs.1c03032.

(20) Yu, B.; Chen, Z.; Zhu, Y.; Wang, Y.; Han, B.; Chen, G.; Zhang, X.; Du, Z.; He, Z. Heterogeneous 2D/3D Tin-Halides Perovskite Solar Cells with Certified Conversion Efficiency Breaking 14%. *Adv. Mater.* **2021**, *33* (36), 2102055. https://doi.org/10.1002/adma.202102055.

(21) Shockley, W.; Queisser, H. J. Detailed Balance Limit of Efficiency of *P-n* Junction Solar Cells. *J. Appl. Phys.* **1961**, *32* (3), 510–519. https://doi.org/10.1063/1.1736034.

(22) Nishikubo, R.; Ishida, N.; Katsuki, Y.; Wakamiya, A.; Saeki, A. Minute-Scale Degradation and Shift of Valence-Band Maxima of (CH3NH3)SnI3 and HC(NH2)2SnI3 Perovskites upon Air Exposure. *J. Phys. Chem. C* **2017**, *121* (36), 19650–19656. https://doi.org/10.1021/acs.jpcc.7b06294.

(23) Jiang, X.; Wang, F.; Wei, Q.; Li, H.; Shang, Y.; Zhou, W.; Wang, C.; Cheng, P.; Chen, Q.; Chen, L.; Ning, Z. Ultra-High Open-Circuit Voltage of Tin Perovskite Solar Cells via an Electron Transporting Layer Design. *Nat. Commun.* **2020**, *11* (1), 1245. https://doi.org/10.1038/s41467-020-15078-2.

(24) Diau, E. W.-G.; Jokar, E.; Rameez, M. Strategies To Improve Performance and Stability for Tin-Based Perovskite Solar Cells. *ACS Energy Lett.* **2019**, *4* (8), 1930–1937. https://doi.org/10.1021/acsenergylett.9b01179.

(25) Li, B.; Chang, B.; Pan, L.; Li, Z.; Fu, L.; He, Z.; Yin, L. Tin-Based Defects and Passivation Strategies in Tin-Related Perovskite Solar Cells. *ACS Energy Lett.* **2020**, *5* (12), 3752–3772. https://doi.org/10.1021/acsenergylett.0c01796.

(26) Jiang, X.; Zang, Z.; Zhou, Y.; Li, H.; Wei, Q.; Ning, Z. Tin Halide Perovskite Solar Cells: An Emerging Thin-Film Photovoltaic Technology. *Acc. Mater. Res.* **2021**, *2* (4), 210–219. https://doi.org/10.1021/accountsmr.0c00111.

(27) Cao, J.; Yan, F. Recent Progress in Tin-Based Perovskite Solar Cells. *Energy Environ. Sci.* **2021**, *14* (3), 1286–1325. https://doi.org/10.1039/D0EE04007J.

(28) Aktas, E.; Rajamanickam, N.; Pascual, J.; Hu, S.; Aldamasy, M. H.; Di Girolamo, D.; Li, W.; Nasti, G.; Martínez-Ferrero, E.; Wakamiya, A.; Palomares, E.; Abate, A. Challenges and Strategies toward Long-Term Stability of Lead-Free Tin-Based Perovskite Solar Cells. *Commun. Mater.* **2022**, *3* (1), 104. https://doi.org/10.1038/s43246-022-00327-2.

(29) Nishimura, K.; Kamarudin, M. A.; Hirotani, D.; Hamada, K.; Shen, Q.; Iikubo, S.; Minemoto, T.; Yoshino, K.; Hayase, S. Lead-Free Tin-Halide Perovskite Solar Cells with 13% Efficiency. *Nano Energy* **2020**, *74*, 104858. https://doi.org/10.1016/j.nanoen.2020.104858.

(30) Liao, Y.; Liu, H.; Zhou, W.; Yang, D.; Shang, Y.; Shi, Z.; Li, B.; Jiang, X.; Zhang, L.; Quan, L. N.; Quintero-Bermudez, R.; Sutherland, B. R.; Mi, Q.; Sargent, E. H.; Ning, Z. Highly Oriented Low-Dimensional Tin Halide Perovskites with Enhanced Stability and Photovoltaic Performance. *J. Am. Chem. Soc.* **2017**, *139* (19), 6693–6699. https://doi.org/10.1021/jacs.7b01815.

(31) Jiang, Y.; Lu, Z.; Zou, S.; Lai, H.; Zhang, Z.; Luo, J.; Huang, Y.; He, R.; Jin, J.; Yi, Z.; Luo, Y.; Wang, W.; Wang, C.; Hao, X.; Chen, C.; Wang, X.; Wang, Y.; Ren, S.; Shi, T.; Fu, F.; Zhao, D. Dual-Site Passivation of Tin-Related Defects Enabling Efficient Lead-Free Tin Perovskite Solar Cells. *Nano Energy* **2022**, *103*, 107818. https://doi.org/10.1016/j.nanoen.2022.107818.

(32) Liu, X.; Wu, T.; Zhang, C.; Zhang, Y.; Segawa, H.; Han, L. Interface Energy-Level Management toward Efficient Tin Perovskite Solar Cells with Hole-Transport-Layer-Free Structure. *Adv. Funct. Mater.* **2021**, *31* (50), 2106560. https://doi.org/10.1002/adfm.202106560.

(33) Lei, Y.; Li, Y.; Lu, C.; Yan, Q.; Wu, Y.; Babbe, F.; Gong, H.; Zhang, S.; Zhou, J.; Wang, R.; Zhang, R.; Chen, Y.; Tsai, H.; Gu, Y.; Hu, H.; Lo, Y.-H.; Nie, W.; Lee, T.; Luo, J.; Yang, K.; Jang, K.-I.; Xu, S. Perovskite Superlattices with Efficient Carrier Dynamics. *Nature* **2022**, *608* (7922), 317–323. https://doi.org/10.1038/s41586-022-04961-1.

(34) Wu, T.; Liu, X.; Luo, X.; Segawa, H.; Tong, G.; Zhang, Y.; Ono, L. K.; Qi, Y.; Han, L. Heterogeneous FASnI3 Absorber with Enhanced Electric Field for High-Performance Lead-Free Perovskite Solar Cells. *Nano-Micro Lett.* **2022**, *14* (1), 99. https://doi.org/10.1007/s40820-022-00842-4.

(35) Wang, T.; Loi, H.; Cao, J.; Qin, Z.; Guan, Z.; Xu, Y.; Cheng, H.; Li, M. G.; Lee, C.; Lu, X.; Yan, F. High Open Circuit Voltage Over 1 V Achieved in Tin-Based Perovskite Solar Cells with a 2D/3D Vertical Heterojunction. *Adv. Sci.* **2022**, 2200242. https://doi.org/10.1002/advs.202200242.

(36) Blakesley, J. C.; Neher, D. Relationship between Energetic Disorder and Open-Circuit Voltage in Bulk Heterojunction Organic Solar Cells. *Phys. Rev. B* **2011**, 12.

(37) Hoffmann, S. T.; Bässler, H.; Köhler, A. What Determines Inhomogeneous Broadening of Electronic Transitions in Conjugated Polymers? *J. Phys. Chem. B* **2010**, *114* (51), 17037–17048. https://doi.org/10.1021/jp107357y.

(38) Lin, Y.; Chen, B.; Zhao, F.; Zheng, X.; Deng, Y.; Shao, Y.; Fang, Y.; Bai, Y.; Wang, C.; Huang, J. Matching Charge Extraction Contact for Wide-Bandgap Perovskite Solar Cells. *Adv. Mater.* **2017**, *29* (26), 1700607. https://doi.org/10.1002/adma.201700607.

(39) Shao, Y.; Yuan, Y.; Huang, J. Correlation of Energy Disorder and Open-Circuit Voltage in Hybrid Perovskite Solar Cells. *Nat. Energy* **2016**, *1* (1), 15001. https://doi.org/10.1038/nenergy.2015.1.

(40) Silinsh, E. A. On the Physical Nature of Traps in Molecular Crystals. *Phys. Status Solidi A* **1970**, *3* (3), 817–828. https://doi.org/10.1002/pssa.19700030329.

(41) Groves, C. Suppression of Geminate Charge Recombination in Organic Photovoltaic Devices with a Cascaded Energy Heterojunction. *Energy Environ. Sci.* **2013**, *6* (5), 1546. https://doi.org/10.1039/c3ee24455e.

(42) Yuan, J.; Zhang, C.; Qiu, B.; Liu, W.; So, S. K.; Mainville, M.; Leclerc, M.; Shoaee, S.; Neher, D.; Zou, Y. Effects of Energetic Disorder in Bulk Heterojunction Organic Solar Cells. *Energy Environ. Sci.* **2022**, *15* (7), 2806–2818. https://doi.org/10.1039/D2EE00271J.

(43) Lv, J.; Tang, H.; Huang, J.; Yan, C.; Liu, K.; Yang, Q.; Hu, D.; Singh, R.; Lee, J.; Lu, S.; Li, G.; Kan, Z. Additive-Induced Miscibility Regulation and Hierarchical Morphology Enable 17.5% Binary Organic Solar Cells. *Energy Environ. Sci.* **2021**, *14* (5), 3044–3052. https://doi.org/10.1039/D0EE04012F.

(44) Tummala, N. R.; Elroby, S. A.; Aziz, S. G.; Risko, C.; Coropceanu, V.; Brédas, J.-L. Packing and Disorder in Substituted Fullerenes. *J. Phys. Chem. C* **2016**, *120* (31), 17242–17250. https://doi.org/10.1021/acs.jpcc.6b05197.

(45) Perdigón-Toro, L.; Phuong, L. Q.; Eller, F.; Freychet, G.; Saglamkaya, E.; Khan, J. I.; Wei, Q.; Zeiske, S.; Kroh, D.; Wedler, S.; Köhler, A.; Armin, A.; Laquai, F.; Herzig, E. M.; Zou, Y.; Shoaee, S.; Neher, D. Understanding the Role of Order in Y-Series Non-Fullerene Solar Cells to Realize High Open-Circuit Voltages. *Adv. Energy Mater.* **2022**, *12* (12), 2103422. https://doi.org/10.1002/aenm.202103422.

(46) Jiang, K.; Wei, Q.; Lai, J. Y. L.; Peng, Z.; Kim, H. K.; Yuan, J.; Ye, L.; Ade, H.; Zou, Y.; Yan, H. Alkyl Chain Tuning of Small Molecule Acceptors for Efficient Organic Solar Cells. *Joule* **2019**, *3* (12), 3020–3033. https://doi.org/10.1016/j.joule.2019.09.010.

(47) Jiang, Y.; Wang, J.; Zai, H.; Ni, D.; Wang, J.; Xue, P.; Li, N.; Jia, B.; Lu, H.; Zhang, Y.; Wang, F.; Guo, Z.; Bi, Z.; Xie, H.; Wang, Q.; Ma, W.; Tu, Y.; Zhou, H.; Zhan, X. Reducing Energy Disorder in Perovskite Solar Cells by Chelation. *J. Am. Chem. Soc.* **2022**, *144* (12), 5400–5410. https://doi.org/10.1021/jacs.1c12732.

(48) Li, H.; Zang, Z.; Wei, Q.; Jiang, X.; Ma, M.; Xing, Z.; Wang, J.; Yu, D.; Wang, F.; Zhou, W.; Wong, K. S.; Chow, P. C. Y.; Zhou, Y.; Ning, Z. High-Member Low-Dimensional Sn-Based Perovskite Solar Cells. *Sci. China Chem.* **2023**, *66* (2), 459–465. https://doi.org/10.1007/s11426-022-1489-8.

(49) Liu, Z.; Xie, X.; Lee, E.-C. Effects of Organic Solvents for the Phenyl-C61-Butyric Acid Methyl Ester Layer on the Performance of Inverted Perovskite Solar Cells. *Org. Electron.* **2018**, *56*, 247–253. https://doi.org/10.1016/j.orgel.2018.02.026.

(50) Wang, M.; Fu, Q.; Yan, L.; Huang, J.; Ma, Q.; Humayun, M.; Pi, W.; Chen, X.; Zheng, Z.; Luo, W. Systematic Optimization of Perovskite Solar Cells via Green Solvent Systems. *Chem. Eng. J.* **2020**, *387*, 123966. https://doi.org/10.1016/j.cej.2019.123966.

(51) Tsai, C.-H.; Lin, C.-M.; Kuei, C.-H. Investigation of the Effects of Various Organic Solvents on the PCBM Electron Transport Layer of Perovskite Solar Cells. *Coatings* **2020**, *10* (3), 237. https://doi.org/10.3390/coatings10030237.

(52) Cho, S.; Pandey, P.; Park, J.; Lee, T.-W.; Kang, D.-W. Mixed Solvent Engineering for Morphology Optimization of the Electron Transport Layer in Perovskite Photovoltaics. *ACS Appl. Energy Mater.* **2022**, *5* (1), 387–396. https://doi.org/10.1021/acsaem.1c02913.

(53) Xia, F.; Wu, Q.; Zhou, P.; Li, Y.; Chen, X.; Liu, Q.; Zhu, J.; Dai, S.; Lu, Y.; Yang, S. Efficiency Enhancement of Inverted Structure Perovskite Solar Cells via Oleamide

Doping of PCBM Electron Transport Layer. *ACS Appl. Mater. Interfaces* **2015**, *7* (24), 13659–13665. https://doi.org/10.1021/acsami.5b03525.

(54) Wu, C.-G.; Chiang, C.-H.; Chang, S. H. A Perovskite Cell with a Record-High-V_{oc} of 1.61 V Based on Solvent Annealed $CH_3NH_3PbBr_3$/ICBA Active Layer. *Nanoscale* **2016**, *8* (7), 4077–4085. https://doi.org/10.1039/C5NR07739G.

(55) Kim, T.; Lim, J.; Song, S. Recent Progress and Challenges of Electron Transport Layers in Organic–Inorganic Perovskite Solar Cells. *Energies* **2020**, *13* (21), 5572. https://doi.org/10.3390/en13215572.

(56) Nilsson, S.; Bernasik, A.; Budkowski, A.; Moons, E. Morphology and Phase Segregation of Spin-Casted Films of Polyfluorene/PCBM Blends. *Macromolecules* **2007**, *40* (23), 8291–8301. https://doi.org/10.1021/ma070712a.

(57) Li, B.; Yu, X.; Jia, L.; Zhang, M.; Hu, W.; Shang, Y.; Li, X.; Ding, L.; Xu, J.; Yang, S. Fast Wetting of a Fullerene Capping Layer Improves the Efficiency and Scalability of Perovskite Solar Cells. *ACS Appl. Mater. Interfaces* **2020**, *12* (33), 37265–37274. https://doi.org/10.1021/acsami.0c11164.

(58) Deng, L.-L.; Xie, S.-Y.; Gao, F. Fullerene-Based Materials for Photovoltaic Applications: Toward Efficient, Hysteresis-Free, and Stable Perovskite Solar Cells. *Adv. Electron. Mater.* **2018**, *4* (10), 1700435. https://doi.org/10.1002/aelm.201700435.

(59) Dai, S.-M.; Zhang, X.; Chen, W.-Y.; Li, X.; Tan, Z.; Li, C.; Deng, L.-L.; Zhan, X.-X.; Lin, M.-S.; Xing, Z.; Wen, T.; Ho, R.-M.; Xie, S.-Y.; Huang, R.-B.; Zheng, L.-S. Formulation Engineering for Optimizing Ternary Electron Acceptors Exemplified by Isomeric PC $_{71}$ BM in Planar Perovskite Solar Cells. *J. Mater. Chem. A* **2016**, *4* (48), 18776–18782. https://doi.org/10.1039/C6TA07750A.

(60) Chang, C.-Y.; Huang, W.-K.; Chang, Y.-C.; Lee, K.-T.; Chen, C.-T. A Solution-Processed n-Doped Fullerene Cathode Interfacial Layer for Efficient and Stable Large-Area Perovskite Solar Cells. *J. Mater. Chem. A* **2016**, *4* (2), 640–648. https://doi.org/10.1039/C5TA09080F.

(61) Elnaggar, M.; Elshobaki, M.; Mumyatov, A.; Luchkin, S. Yu.; Dremova, N. N.; Stevenson, K. J.; Troshin, P. A. Molecular Engineering of the Fullerene-Based Electron Transport Layer Materials for Improving Ambient Stability of Perovskite Solar Cells. *Sol. RRL* **2019**, *3* (9), 1900223. https://doi.org/10.1002/solr.201900223.

(62) Ha, S. R.; Yoon, S.; Eom, S.; Jeong, W. H.; Woo, J.; Yang, J.; Sung, D.; Oh, J. T.; Jeong, H. I.; Choi, W. I.; Kang, Y.; Lee, B. R.; Kang, D.-W.; Choi, H. Multi-Scalable Grain Growth via Phenyl-C $_{60}$ -Butyric Acid Methyl Ester Molecular Aggregation in Perovskite Solar Cells. *ACS Appl. Energy Mater.* **2021**, *4* (6), 5985–5994. https://doi.org/10.1021/acsaem.1c00826.

(63) Bässler, H. Charge Transport in Disordered Organic Photoconductors a Monte Carlo Simulation Study. *Phys. Status Solidi B* **1993**, *175* (1), 15–56. https://doi.org/10.1002/pssb.2221750102.

(64) Xu, G.; Xue, R.; Stuard, S. J.; Ade, H.; Zhang, C.; Yao, J.; Li, Y.; Li, Y. Reducing Energy Disorder of Hole Transport Layer by Charge Transfer Complex for High Performance p–i–n Perovskite Solar Cells. *Adv. Mater.* **2021**, *33* (13), 2006753. https://doi.org/10.1002/adma.202006753.

(65) Mott N. F.; Gurney R. W. Electronic Processes in Ionic Crystals. *Oxf. Univ. Press* **1940**.

(66) Nakamura, T.; Yakumaru, S.; Truong, M. A.; Kim, K.; Liu, J.; Hu, S.; Otsuka, K.; Hashimoto, R.; Murdey, R.; Sasamori, T.; Kim, H. D.; Ohkita, H.; Handa, T.; Kanemitsu, Y.; Wakamiya, A. Sn(IV)-Free Tin Perovskite Films Realized by in Situ Sn(0) Nanoparticle Treatment of the Precursor Solution. *Nat. Commun.* **2020**, *11* (1), 3008. https://doi.org/10.1038/s41467-020-16726-3.

(67) Choi, W.-G.; Park, C.-G.; Kim, Y.; Moon, T. Sn Perovskite Solar Cells via 2D/3D Bilayer Formation through a Sequential Vapor Process. *ACS Energy Lett.* **2020**, *5* (11), 3461–3467. https://doi.org/10.1021/acsenergylett.0c01887.

(68) Chen, M.; Dong, Q.; Eickemeyer, F. T.; Liu, Y.; Dai, Z.; Carl, A. D.; Bahrami, B.; Chowdhury, A. H.; Grimm, R. L.; Shi, Y.; Qiao, Q.; Zakeeruddin, S. M.; Grätzel, M.; Padture, N. P. High-Performance Lead-Free Solar Cells Based on Tin-Halide

Perovskite Thin Films Functionalized by a Divalent Organic Cation. *ACS Energy Lett.* **2020**, *5* (7), 2223–2230. https://doi.org/10.1021/acsenergylett.0c00888.

(69) Li, B.; Di, H.; Chang, B.; Yin, R.; Fu, L.; Zhang, Y.; Yin, L. Efficient Passivation Strategy on Sn Related Defects for High Performance All-Inorganic $CsSnI_3$ Perovskite Solar Cells. *Adv. Funct. Mater.* **2021**, *31* (11), 2007447. https://doi.org/10.1002/adfm.202007447.

(70) Cui, D.; Liu, X.; Wu, T.; Lin, X.; Luo, X.; Wu, Y.; Segawa, H.; Yang, X.; Zhang, Y.; Wang, Y.; Han, L. Making Room for Growing Oriented $FASnI_3$ with Large Grains via Cold Precursor Solution. *Adv. Funct. Mater.* **2021**, *31* (25), 2100931. https://doi.org/10.1002/adfm.202100931.

(71) Chen, M.; Kamarudin, M. A.; Baranwal, A. K.; Kapil, G.; Ripolles, T. S.; Nishimura, K.; Hirotani, D.; Sahamir, S. R.; Zhang, Z.; Ding, C.; Sanehira, Y.; Bisquert, J.; Shen, Q.; Hayase, S. High-Efficiency Lead-Free Wide Band Gap Perovskite Solar Cells via Guanidinium Bromide Incorporation. *ACS Appl. Energy Mater.* **2021**, *4* (6), 5615–5624. https://doi.org/10.1021/acsaem.1c00413.

(72) Zhou, J.; Hao, M.; Zhang, Y.; Ma, X.; Dong, J.; Lu, F.; Wang, J.; Wang, N.; Zhou, Y. Chemo-Thermal Surface Dedoping for High-Performance Tin Perovskite Solar Cells. *Matter* **2022**, *5* (2), 683–693. https://doi.org/10.1016/j.matt.2021.12.013.

(73) Wang, C.; Zhang, Y.; Gu, F.; Zhao, Z.; Li, H.; Jiang, H.; Bian, Z.; Liu, Z. Illumination Durability and High-Efficiency Sn-Based Perovskite Solar Cell under

Coordinated Control of Phenylhydrazine and Halogen Ions. *Matter* **2021**, *4* (2), 709–721. https://doi.org/10.1016/j.matt.2020.11.012.

(74) Hao, F.; Stoumpos, C. C.; Cao, D. H.; Chang, R. P. H.; Kanatzidis, M. G. Lead-Free Solid-State Organic–Inorganic Halide Perovskite Solar Cells. *Nat. Photonics* **2014**, *8* (6), 489–494. https://doi.org/10.1038/nphoton.2014.82.

(75) Wang, C.; Gu, F.; Zhao, Z.; Rao, H.; Qiu, Y.; Cai, Z.; Zhan, G.; Li, X.; Sun, B.; Yu, X.; Zhao, B.; Liu, Z.; Bian, Z.; Huang, C. Self-Repairing Tin-Based Perovskite Solar Cells with a Breakthrough Efficiency Over 11%. *Adv. Mater.* **2020**, *32* (31), 1907623. https://doi.org/10.1002/adma.201907623.

(76) Li, B.; Wu, X.; Zhang, H.; Zhang, S.; Li, Z.; Gao, D.; Zhang, C.; Chen, M.; Xiao, S.; Jen, A. K. -Y.; Yang, S.; Zhu, Z. Efficient and Stable Tin Perovskite Solar Cells by Pyridine-Functionalized Fullerene with Reduced Interfacial Energy Loss. *Adv. Funct. Mater.* **2022**, *32* (39), 2205870. https://doi.org/10.1002/adfm.202205870.

(77) Zou, S.; Ren, S.; Jiang, Y.; Huang, Y.; Wang, W.; Wang, C.; Chen, C.; Hao, X.; Wu, L.; Zhang, J.; Zhao, D. Efficient Environment-friendly Lead-free Tin Perovskite Solar Cells Enabled by Incorporating 4-FLUOROBENZYLAMMONIUM Iodide Additives. *ENERGY Environ. Mater.* **2022**. https://doi.org/10.1002/eem2.12465.

(78) Zhu, Z.; Jiang, X.; Yu, D.; Yu, N.; Ning, Z.; Mi, Q. Smooth and Compact $FASnI_3$ Films for Lead-Free Perovskite Solar Cells with over 14% Efficiency. *ACS Energy Lett.* **2022**, *7* (6), 2079–2083. https://doi.org/10.1021/acsenergylett.2c00776.

(79) Wang, L.; Chen, M.; Yang, S.; Uezono, N.; Miao, Q.; Kapil, G.; Baranwal, A. K.; Sanehira, Y.; Wang, D.; Liu, D.; Ma, T.; Ozawa, K.; Sakurai, T.; Zhang, Z.; Shen, Q.; Hayase, S. SnO_x as Bottom Hole Extraction Layer and Top In Situ Protection Layer Yields over 14% Efficiency in Sn-Based Perovskite Solar Cells. *ACS Energy Lett.* **2022**, *7* (10), 3703–3708. https://doi.org/10.1021/acsenergylett.2c01659.

(80) Perini, C. A. R.; Rojas-Gatjens, E.; Ravello, M.; Castro-Mendez, A.; Hidalgo, J.; An, Y.; Kim, S.; Lai, B.; Li, R.; Silva-Acuña, C.; Correa-Baena, J. Interface Reconstruction from Ruddlesden–Popper Structures Impacts Stability in Lead Halide Perovskite Solar Cells. *Adv. Mater.* **2022**, *34* (51), 2204726. https://doi.org/10.1002/adma.202204726.

(81) Li, X.; Hoffman, J. M.; Kanatzidis, M. G. The 2D Halide Perovskite Rulebook: How the Spacer Influences Everything from the Structure to Optoelectronic Device Efficiency. *Chem. Rev.* **2021**, *121* (4), 2230–2291. https://doi.org/10.1021/acs.chemrev.0c01006.

(82) Dong, H.; Ran, C.; Gao, W.; Sun, N.; Liu, X.; Xia, Y.; Chen, Y.; Huang, W. Crystallization Dynamics of Sn-Based Perovskite Thin Films: Toward Efficient and Stable Photovoltaic Devices. *Adv. Energy Mater.* **2022**, *12* (1), 2102213. https://doi.org/10.1002/aenm.202102213.

(83) Krückemeier, L.; Rau, U.; Stolterfoht, M.; Kirchartz, T. How to Report Record Open-Circuit Voltages in Lead-Halide Perovskite Solar Cells. *Adv. Energy Mater.* **2020**, *10* (1), 1902573. https://doi.org/10.1002/aenm.201902573.

(84) Rühle, S. Tabulated Values of the Shockley–Queisser Limit for Single Junction Solar Cells. *Sol. Energy* **2016**, *130*, 139–147. https://doi.org/10.1016/j.solener.2016.02.015.

(85) Correa-Baena, J.-P.; Saliba, M.; Buonassisi, T.; Grätzel, M.; Abate, A.; Tress, W.; Hagfeldt, A. Promises and Challenges of Perovskite Solar Cells. *Science* **2017**, *358* (6364), 739–744. https://doi.org/10.1126/science.aam6323.

(86) Luo, D.; Su, R.; Zhang, W.; Gong, Q.; Zhu, R. Minimizing Non-Radiative Recombination Losses in Perovskite Solar Cells. *Nat. Rev. Mater.* **2019**, *5* (1), 44–60. https://doi.org/10.1038/s41578-019-0151-y.

(87) Wu, T.; Liu, X.; Luo, X.; Lin, X.; Cui, D.; Wang, Y.; Segawa, H.; Zhang, Y.; Han, L. Lead-Free Tin Perovskite Solar Cells. *Joule* **2021**, *5* (4), 863–886. https://doi.org/10.1016/j.joule.2021.03.001.

(88) Lanzetta, L.; Webb, T.; Zibouche, N.; Liang, X.; Ding, D.; Min, G.; Westbrook, R. J. E.; Gaggio, B.; Macdonald, T. J.; Islam, M. S.; Haque, S. A. Degradation Mechanism of Hybrid Tin-Based Perovskite Solar Cells and the Critical Role of Tin (IV) Iodide. *Nat. Commun.* **2021**, *12* (1), 2853. https://doi.org/10.1038/s41467-021-22864-z.

(89) Huang, H.-H.; Tsai, H.; Raja, R.; Lin, S.-L.; Ghosh, D.; Hou, C.-H.; Shyue, J.-J.; Tretiak, S.; Chen, W.; Lin, K.-F.; Nie, W.; Wang, L. Robust Unencapsulated Perovskite Solar Cells Protected by a Fluorinated Fullerene Electron Transporting Layer. *ACS Energy Lett.* **2021**, *6* (9), 3376–3385. https://doi.org/10.1021/acsenergylett.1c01526.

(90) Liu, K.; Chen, S.; Wu, J.; Zhang, H.; Qin, M.; Lu, X.; Tu, Y.; Meng, Q.; Zhan, X. Fullerene Derivative Anchored SnO_2 for High-Performance Perovskite Solar Cells. *Energy Environ. Sci.* **2018**, *11* (12), 3463–3471. https://doi.org/10.1039/C8EE02172D.

(91) Hu, S.; Otsuka, K.; Murdey, R.; Nakamura, T.; Truong, M. A.; Yamada, T.; Handa, T.; Matsuda, K.; Nakano, K.; Sato, A.; Marumoto, K.; Tajima, K.; Kanemitsu, Y.; Wakamiya, A. Optimized Carrier Extraction at Interfaces for 23.6% Efficient Tin–Lead Perovskite Solar Cells. *Energy Environ. Sci.* **2022**, *15* (5), 2096–2107. https://doi.org/10.1039/D2EE00288D.

(92) Hu, S.; Pascual, J.; Liu, W.; Funasaki, T.; Truong, M. A.; Hira, S.; Hashimoto, R.; Morishita, T.; Nakano, K.; Tajima, K.; Murdey, R.; Nakamura, T.; Wakamiya, A. A Universal Surface Treatment for p–i–n Perovskite Solar Cells. *ACS Appl. Mater. Interfaces* **2022**, *14* (50), 56290–56297. https://doi.org/10.1021/acsami.2c15989.

TOC

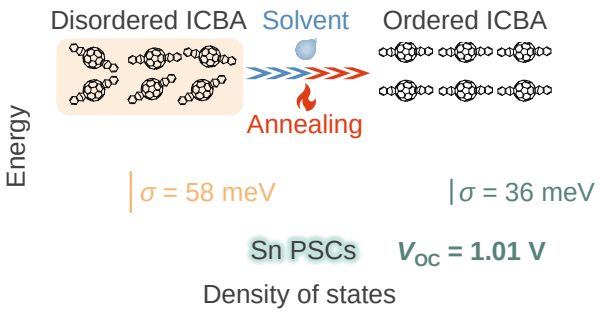
Disordered ICBA
Solvent
Ordered ICBA
Annealing
Energy
σ = 58 meV
σ = 36 meV
Sn PSCs
V_{OC} = 1.01 V
Density of states